

www.acsami.org Research Article

Atomic Dislocations and Bond Rupture Govern Dissolution Enhancement under Acoustic Stimulation

Longwen Tang,[&] Shiqi Dong,[&] Ross Arnold, Erika Callagon La Plante, Juan Carlos Vega-Vila, Dale Prentice, Kirk Ellison, Aditya Kumar, Narayanan Neithalath, Dante Simonetti, Gaurav Sant,* and Mathieu Bauchy*



Cite This: ACS Appl. Mater. Interfaces 2020, 12, 55399–55410



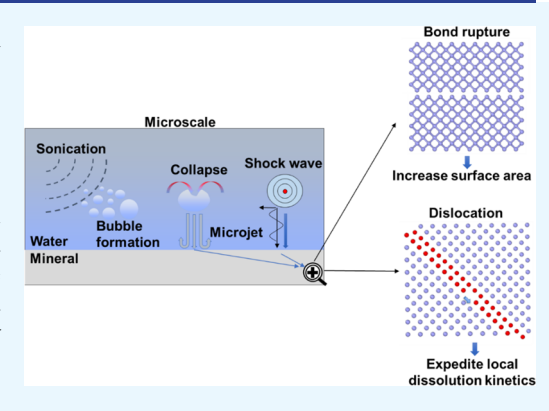
ACCESS

Metrics & More

Article Recommendations

s Supporting Information

ABSTRACT: By focusing the power of sound, acoustic stimulation (i.e., often referred to as sonication) enables numerous "green chemistry" pathways to enhance chemical reaction rates, for instance, of mineral dissolution in aqueous environments. However, a clear understanding of the atomistic mechanism(s) by which acoustic stimulation promotes mineral dissolution remains unclear. Herein, by combining nanoscale observations of dissolving surface topographies using vertical scanning interferometry, quantifications of mineral dissolution rates via analysis of solution compositions using inductively coupled plasma optical emission spectrometry, and classical molecular dynamics simulations, we reveal how acoustic stimulation induces dissolution enhancement. Across a wide range of minerals (Mohs hardness ranging from 3 to 7, surface energy ranging from 0.3 to 7.3 J/m², and stacking fault energy ranging from 0.8 to 10.0 J/m²), we show that acoustic fields enhance mineral dissolution rates (reactivity) by inducing atomic dislocations and/or atomic bond rupture.



The relative contributions of these mechanisms depend on the mineral's underlying mechanical properties. Based on this new understanding, we create a unifying model that comprehensively describes how cavitation and acoustic stimulation processes affect mineral dissolution rates.

KEYWORDS: acoustic stimulation, mineral dissolution, molecular dynamics simulations, activation energy, atomic bond rupture

INTRODUCTION

When high-intensity (i.e., energy per unit volume) ultrasound is transmitted through a liquid, microscale bubbles form, grow, and collapse. 1,2 The collapse of microscale bubbles causes the formation of shock waves or high-velocity microjets, which can locally induce high pressures (up to several GPa)³ and impart mechanical energy (up to dozens of mJ per bubble)⁴ onto adjoining surfaces and interfaces. This can damage the surfaces of immersed solids, 5,6 e.g., ship propellers and hydraulic turbines. 7,8 On the other hand, such energetic perturbations offer a cost-efficient, reagent-free route to promote mineral dissolution, radical formation, etc., while mitigating energy consumption and toxic reagent requirements. 9-12 Therefore, sonication promotes "green chemistry" approaches for control and affectation of chemical reactions. The enhanced dissolution of inorganic minerals and solids is of interest for numerous applications, e.g., to enhance the beneficial utilization of industrial by-products (e.g., slags and fly ash) and rocks and to promote CO2 mineralization, for rare-earth element extraction, or other species used as precursors for zeolite synthesis, etc. 13,14 Each of these approaches is foundational to achieve waste utilization and CO2 mitigation

(and utilization) and to broadly promote the principles and mandate of circular economy.

In spite of the many benefits and associated anecdotal observations, our understanding of the mechanisms of action—i.e., by which acoustic stimulation promotes mineral dissolution—has remained uncertain. For example, the increase in reactivity upon sonication has often been attributed to a "temperature effect", which arises from the high temperature achieved within cavitation bubbles. However, recent results have suggested that even under isothermal (i.e., macroscopically thermostatic) conditions, the effects of sonication are substantive. On the other hand, sonication has been thought to impose a "pressure effect", wherein the pressure resulting from the shock waves deforms or fractures solid surfaces. Finally, the increase in dissolution kinetics

Received: September 11, 2020 Accepted: November 20, 2020 Published: December 1, 2020





Table 1. Minerals Studied Herein along with Their Dissolution Rates under Nonsonicated and Sonicated Conditions and Their Relative Increases in Dissolution Rate upon Sonication^a

mineral (25 °C, 1 bar)	nonsonicated dissolution rate ($\times 10^{-9} \text{ mol/m}^2/\text{s}$)	sonicated dissolution rate ($\times 10^{-9} \text{ mol/m}^2/\text{s}$)	relative increase in dissolution
albite (NaAlSi ₃ O ₈)	3.80 ± 0.42	18.9 ± 2.0	$400\pm86\%$
anorthite (CaAl ₂ Si ₂ O ₈)	9.10 ± 0.67	22.4 ± 1.5	$150\pm22\%$
antigorite $(Mg_3(Si_2O_5)(OH)_4)$	4.50 ± 0.52	60.9 ± 5.8	$1300 \pm 270\%$
calcite (CaCO ₃)	1950 ± 190	9400 ± 680	$380 \pm 65\%$
dolomite (Ca,Mg(CO ₃) ₂)	256 ± 49	1590 ± 190	$520 \pm 160\%$
fluorite (CaF ₂)	491 ± 28	1960 ± 210	$300 \pm 50\%$
orthoclase (KAlSi ₃ O ₈)	4.51 ± 0.52	19.7 ± 1.3	$340 \pm 62\%$
α -quartz (SiO ₂)	27.0 ± 1.7	28.8 ± 1.0	$6.50 \pm 0.63\%$
^a Dissolution rates are averaged over two independent measurements.			

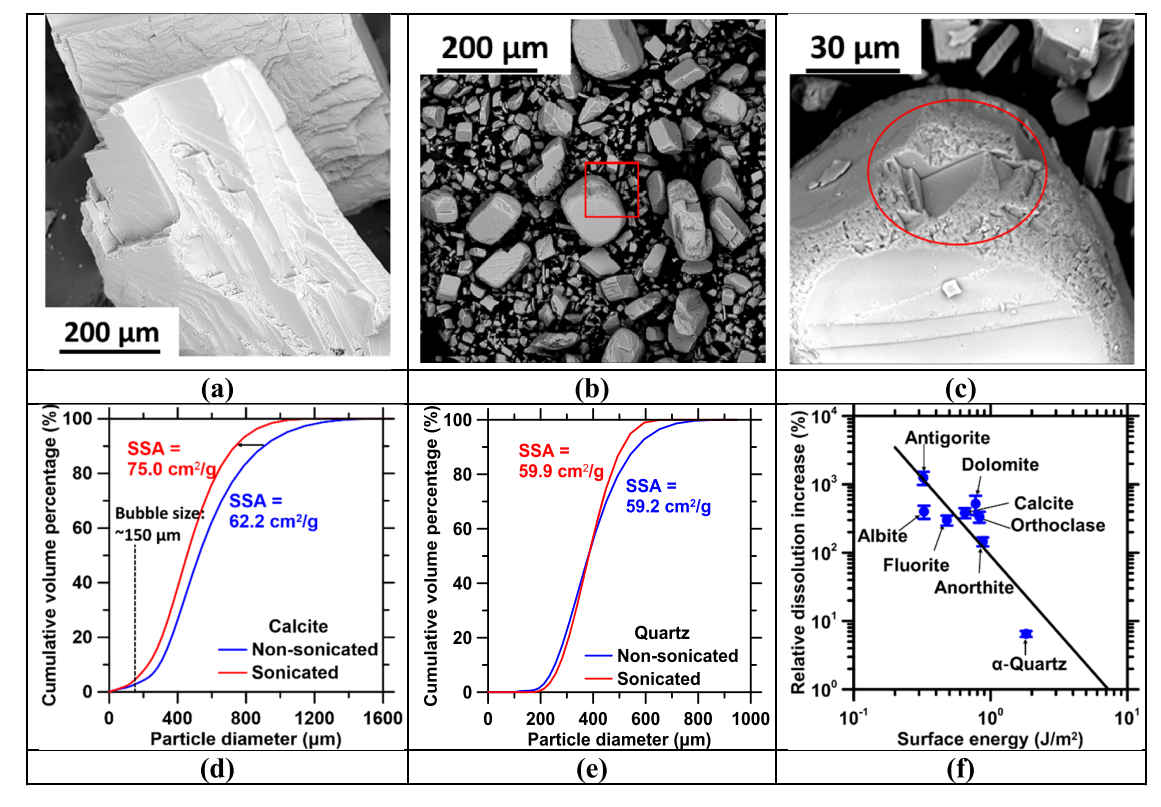


Figure 1. Effect of particulate fracture on dissolution enhancement. Morphology images of calcite particulates following 30 min of dissolution under (a) nonsonicated and (b, c) sonicated conditions, as observed by scanning electron microscopy (SEM). The corner of one particulate labeled with a red square in (b) is enlarged and shown in (c) and exhibits smoothened edges and a newly formed sharp concave corner (red circle). Cumulative volume distribution of solute particulates following 30 min of dissolution under nonsonicated and sonicated conditions for (d) calcite and (e) quartz. The vertical dashed line in (d) indicates the estimated average size of collapsing bubbles.³¹ (f) Measured relative increase in dissolution rate (D_r) as a function of the surface energy computed by molecular dynamics simulations for all the minerals considered herein. In (f), the data are fitted by an equation of the form $\log(D_r) = -2.27 \log(\gamma_{\rm surf}) + 4.50$, where $\gamma_{\rm surf}$ (J/m²) is the surface energy of the solute. The error bars represent the standard deviation.

upon sonication has been postulated to be on account of improved mass transfer in solution, especially at solid—liquid interfaces due to mixing. However, for equivalent conditions of convection (i.e., at constant Reynolds number *Re*), the dissolution enhancement produced by convection alone is substantively inferior to that resulting from sonication. Reprote these reasons, it is necessary to mechanistically unravel how the chemical composition, structure, and properties of the mineral solute and the imposed attributes of the acoustic field affect the enhancement in dissolution rate that results upon sonication. As a complement to experiments, molecular dynamics simulations (MD) can provide a direct access to the effect of sonication on materials at the atomic scale and over a

typical timescale of a few nanoseconds—which is largely invisible to experiments. The formation of dislocations in crystals subjected to a shock impact can be directly observed using nonequilibrium MD simulations. ^{6,22,23} In addition, the dynamics of the collapse of nanobubbles formed upon sonication can also be described by MD simulations. ^{24,25}

In this study, we seek to investigate the nature of the underlying mechanism(s) that controls the enhancement in dissolution kinetics featured by minerals upon sonication and, based on this knowledge, to establish a predictive model describing the effect of sonication on dissolution kinetics. To this end, we identify the key material properties that govern the potential for sonication to accelerate dissolution. Specifically,

we show that the acoustic stimulation affects minerals' reactivity through the breaking of interatomic bonds and the formation of atomic dislocations. Based on these results, we introduce a new framework to describe the effects of sonication on minerals' dissolution. This model rationalizes and explains the effects of acoustic stimulation on mineral reactivity as a combinatorial effect associated with atomic dislocations and bond breaking and offers a unique framework to describe the effects of bubble cavitation on interfacial dissolution processes.

■ RESULTS AND DISCUSSION

Effect of Sonication on Dissolution Kinetics. We focused on eight archetypical minerals (see Table 1)—chosen based on their abundance in Earth's crust²⁶ and so as to cover a wide range of mineral families and crystal classes (see Table S1). We measured their far-from-equilibrium dissolution rates both under sonicated (acoustically stimulated) and non-stimulated conditions (see Methods). To quantify the effects of acoustic stimulation on reactivity, we ascertained the relative increase in dissolution rate under stimulation as

$$D_{\rm r}(\%) = \frac{k_{\rm s} - k_0}{k_0} \times 100\% \tag{1}$$

where k_s and k_0 are the dissolution rates measured under stimulated and stimulation-free conditions, respectively. As observed previously, we find that acoustic stimulation systematically enhances dissolution rates (see Table 1). However, we observe that the effect of stimulation on dissolution significantly depends on the mineral. For instance, the relative increase in dissolution rate ranges from 6.5% for quartz (i.e., wherein the effect of sonication is negligible) to 1300% for antigorite (i.e., a notable 14× increase). In line with previous observations, 18 this demonstrates that the magnitude of stimulation-induced dissolution acceleration is strongly solute-dependent. Note that to enable meaningful comparisons, (i) for the dissolution analyses, all analyses are uniformly conducted under isothermal conditions (25 \pm 0.5 °C) and (ii) the stimulation-free analyses are carried out under matched conditions of convective mixing (of equivalent Reynolds number).¹⁸ When considered within this context, the data in Table 1 highlight that the dissolution amplifications produced by acoustic stimulation are not on account of bulk heating and/or convection, as previously suggested.^{27,28}

Role of Surface Area Increase Caused by Particulate Fracture. We now seek to assess whether the stimulated dissolution acceleration arises from an increase in the exposed surface area of dissolving solids (e.g., due to fracture or deformation). Indeed, the collapse of cavitation bubbles can generate surface stresses on solid surfaces, which may, for instance, result in surface damage and fracture.²⁹ Therefore, we first examined, superficially, the shape, size, and morphology of solid particulates (i.e., around four to six particulates of antigorite, calcite, and quartz; shown in Figure S1 in the Supporting Information) prior to and following 30 min of dissolution under conditions of acoustic stimulation for solids that show high, intermediate, and low sensitivity to acoustic stimulation, respectively (see Table 1). We observed that antigorite and calcite particulates have small "chips" broken off and that the edges and corners of the antigorite and calcite particulates became smoother following stimulation due to interactions with high-velocity microjets. ³⁰ In contrast, the quartz particles appear virtually unaffected by sonication (see

Figure S1 in the Supporting Information). While qualitative, these observations—although coarse—are consistent with the fact that the dissolution kinetics of quartz are broadly unaffected by acoustic stimulation. The morphology changes of calcite particulate following dissolution are augmented by scanning electron microscopy (SEM). Following nonsonicated dissolution, calcite particulates exhibit well-defined cleavage edges and planes, which are formed during sample preparation, i.e., mechanical grinding (see Figure 1a). However, these edges and corners become smoothened after dissolution under sonication (see Figure 1b). One the one hand, the implosion of cavitation bubbles tends to break the calcite particulates into smaller pieces. For example, in Figure 1b, the dimension of the majority of the particulates becomes lower than 300 μ m, wherein many particulates have a size below 50 μ m. The smaller-sized pieces are likely to be flaked off from the corner and/or edges of the original particulates—as shown in Figure 1c, which highlights a newly formed sharp concave corner (red circle) of a particulate present in Figure 1b (labeled with red square). On the other hand, the high-frequency interparticle collisions driven by ultrasound tend to accelerate the rounding of the newly formed cleavage edges and planes and therefore facilitate the smoothening of the edges and corners.³¹ These observations suggest that sonication-induced fracture—and resulting changes in the surface of the particles—might impact their dissolution kinetics.

To more quantitatively validate our visual observations, we measured the particle size distribution (PSD) of stimulated and nonstimulated dissolving particulates (see Methods). First, we note that the PSD of the solute remains effectively unchanged over the time period of nonsonicated dissolution (see Figure S2). For example, even for calcite (i.e., the mineral that exhibits the fastest dissolution kinetics among the solutes considered herein, see Table 1), 30 min of nonsonicated dissolution reduces the size of a median particle ($d_{50} \approx 493.6$ μ m) by at most 0.13 μ m, which is negligible as compared to its pristine dimension. In contrast, as shown in Figure 1d, the PSD features a considerable leftward shift upon sonication, which is indicative of particle size reduction. For example, for calcite, we note reduction in particle diameters of nearly 100 μ m (see Figure 1d). Based on the dissolution rate measured under sonicated conditions $(9.40 \times 10^{-6} \text{ mol/m}^2/\text{s})$ and the short reaction time of 30 min, this decrease in particle size cannot be explained solely by amplified dissolution. Rather, sonication appears to induce significant fracture and comminution wherein calcite particulates break into smaller pieces. Such a fracture results in a 20% increase in specific surface area (SSA) of calcite (see Figure 1d; as measured using light scattering data and assuming spherical particles), which, in turn, is expected to result in a proportionate increase in its dissolution rate—although not to the extent shown in Table 1 (see below). For reference, herein (20 kHz ultrasound), the collapsing cavitation bubbles are estimated to have an average diameter of \sim 150 μ m, ³¹ as labeled with a black vertical dashed line in Figure 1d. We find that the shift in PSD resulting from sonication is notably more pronounced for the particulates exhibiting a diameter that is larger than the average bubble size. This suggests that the fracture of the particulates upon sonication is primarily on account of asymmetric bubble collapse and microjet formation. 18,31,32 It is noted that the shift in the PSD curve in the small particle diameter region might be underestimated as the small flakes (see Figure 1b) cannot be completely retrieved from solution. Nevertheless, in contrast

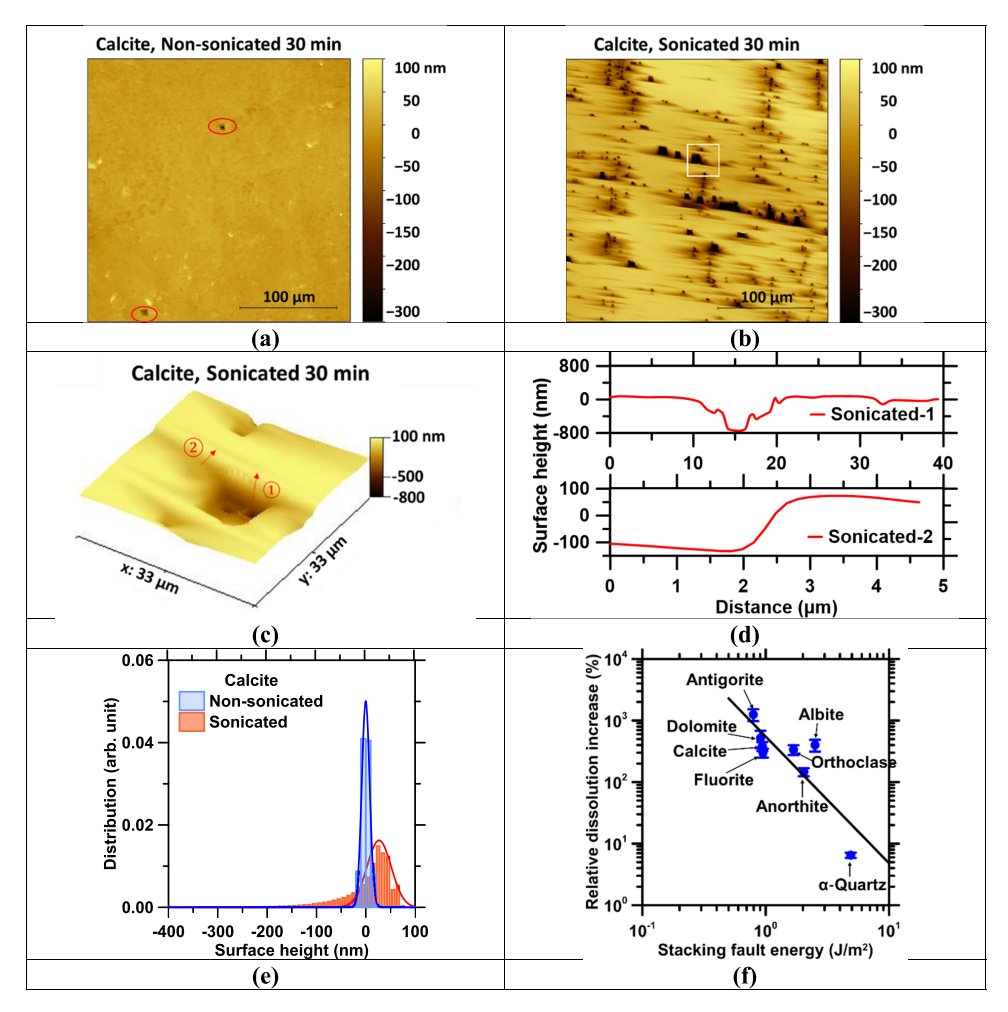


Figure 2. Effect of sonication on the topography of dissolving calcite surfaces. (a, b) Representative topography images of calcite surfaces following 30 min of dissolution under (a) nonsonicated and (b) sonicated conditions. Etch pits developed under nonsonicated dissolution are marked with red circles in (a). (d) 3D topography map and (e) surface height line profiles of representative pits that are marked with a white box in (b). (e) Associated surface height frequency distributions, wherein the solid lines show Gaussian fits. The mean height in each topography profile is normalized to be 0 nm. (f) Measured relative increase in dissolution rate (D_r) as a function of the stacking fault energy computed by molecular dynamics simulations for all the minerals considered herein. In (f), the data are fitted by an equation of the form $\log(D_r) = -2.06 \log(\gamma_{\text{fault}}) + 6.30$, where γ_{fault} is the stacking fault energy (I/m^2) for a given solute. The error bars represent the standard deviation.

with calcite, the PSD of quartz shows a surface area increase of only around 1% (see Figure 1e), which could also be due to variations within samples. This explains, at least in part, the differing effects of acoustic stimulation on the dissolution behavior of calcite and quartz. More broadly, these results suggest that sonication-induced fracture is at least partially at the origin of the dissolution rate amplification observed herein.

To better understand the linkages between sonication-induced dissolution acceleration and solute fracture, for the range of solutes considered herein, molecular dynamics (MD) simulations were used to compute their surface energy in vacuum (see Methods) along the cleavage surface of the minerals—i.e., the weakest surface along which cracks are expected to propagate. Indeed, following linear elastic fracture mechanics (i.e., assuming brittle fracture), the fracture energy required to propagate a preexisting surface flaw is approximately equal to the energy needed to create new surfaces (i.e., two times the surface energy; γ_{surf}).³³ For a fixed energy provided via cavitation (N.B., since for monochromated ultrasound, the mechanical energy arising from cavitation at a given temperature is fixed at constant sonication power), the surface energy captures the relative propensity for minerals to

crack/fracture under sonication. As shown in Figure 1f, we observe a strong, although inverse, correlation (solid black line) between the extent of dissolution acceleration as a function of the mineral's surface energy. This observation implicates the role of fracture in the dissolution stimulation, wherein minerals associated with lower surface energy tend to break more easily, hence revealing additional surface area, and as a result, are more affected by sonication. Nevertheless, the increase in exposed surface area upon sonication remains disproportionately inferior (around 20%) to the observed increase in dissolution rate (about 300% for calcite), in agreement with the conclusions of Wei *et al.*¹⁸ This indicates that, besides fracture, additional acoustic stimulation-activated mechanisms are operative.

Role of Localized Expedited Dissolution Kinetics. To further probe how sonication affects the solute's surface, we used vertical scanning interferometry to examine the evolution of the surface topography of calcite and quartz under sonicated and nonsonicated conditions (see Methods). We first focus on calcite. As shown in Figure S3 (in the Supporting Information), pristine calcite surfaces (i.e., before dissolution) are rather smooth—with a root mean square (RMS) roughness

that is on the order of 5 nm. After 30 min of nonsonicated dissolution, we find that the surface roughness increases up to 10 nm. As shown in Figure 2a, we observe the formation of a few deep etch pits—with local regions deeper than 200 nm—on the dissolving surface. We then calculate the distribution of the pixel-wise heights of the surface both before and after dissolution (see Figure 2e, blue bar plot). We observe that these distributions are largely symmetric. Importantly, we note that nonsonicated dissolution does not notably affect the width of the surface height distribution at the nanometer level. This suggests that within the exposure time period (30 min) under nonsonicated dissolution, the dissolving surface exhibits a fairly homogeneous form of "layer-by-layer" retreat, i.e., each point of the surface dissolves at similar rates and only a few etch pits are formed³⁴—as labeled with red circles in Figure 2a.

In contrast, sonicated dissolution results in the formation of a significantly higher number of characteristic rhombohedral etch pits (see Figure 2b). For example, Figure 2c illustrates the local topography of a typical etch pit that shows a depth of about 800 nm and a lateral (equiaxed) width of around 5 μ m (see Figure 2d, line 1). In addition, we observe the systematic existence of a fast-dissolving region surrounding each pit (see the directional dark brown areas in Figure 2b). In line with the stepwave model, these areas are formed by dissolution waves emanating from an etch pit.³⁵ An example of this behavior is illustrated in Figure 2d (line 2), which shows a fast-dissolving area up to 200 nm deep that is around 10× deeper than the local height variance on the calcite surface following nonsonicated dissolution. The pits (and associated fast-dissolving areas surrounding each pit) forming under sonication result in a large degree of spatial heterogeneity in the local dissolution rate over the calcite surface. This is apparent from the distribution of the pixel-wise surface height (Figure 2e, orange bar plot), which exhibits a wide, nonsymmetric shape, with a long tail toward negative height, indicating fast-dissolving regions. The formation of deep etch pits is also observed for fluorite, which, like calcite, exhibits a notable increase in dissolution kinetics upon sonication (see Figure S8 in the Supporting Information for more details). Overall, the notable difference in the topographies of the calcite and fluorite surfaces—in the presence and absence of acoustic stimulation—suggests that the enhanced propensity for pit formation largely explains the sonication-induced dissolution acceleration. This is further confirmed by the fact that, in contrast, quartz does not exhibit any notable signature of pit formation under sonication (see Figures S4 and S5), which echoes the fact that the dissolution kinetics of quartz are very weakly affected by sonication (Table 1).

The effect of sonication on pit formation can be understood as follows. Under sonication, shock waves or microjets induced by the collapse of cavitation bubbles cause severe local plastic deformations. It should be noted that such plastic deformations differ from the fracture effects illustrated in Figure 1 since they consist of spatially distributed atomic dislocations rather than crack propagation.⁶ These spatially distributed dislocations serve as initiation sites for dislocation etching and, eventually, etch pit formation and growth.^{36,37} The strain energy resulting from such irreversible deformations results in a Gibbs free energy penalty, which, in turn, promotes local dissolution.^{35,38,39} In contrast to the formation of vacancy islands (i.e., pits forming on an atomically smooth surface),³⁷ dislocation etch pits are more likely to develop alongside preexisting defects and result in the formation of deeper (than

typical) pits; for instance, see the comparison of the calcite dissolving surfaces in Figure 2a,b. ⁴⁰ Based on this mechanism, sonication-induced atomic dislocations (and the associated plastic deformations) are key to understanding how sonication accelerates dissolution.

To further demonstrate the role of atomic dislocations in sonication-induced dissolution acceleration, we compute the stacking fault energy of the minerals considered herein using MD simulations (see Methods). The stacking fault energy quantitatively captures the propensity for a mineral to form dislocations under applied surface stress,41 wherein lower stacking fault energies indicate that the formation of atomic dislocations is facilitated (i.e., due to a low energy cost). As shown in Figure 2f, we observe a strong inverse relationship (black solid line) between the extent of dissolution acceleration upon sonication and the stacking fault energy. This confirms that low stacking fault energy (and, hence, the facilitation of atomic dislocations) tends to promote sonication-induced dissolution acceleration. In that regard, it is notable that albite acts as an outlier in Figure 2f-since it exhibits a fairly large increase in dissolution kinetics upon sonication despite showing a large stacking fault energy. In fact, albite's large stacking fault energy is consistent with the fact that like in the case of quartz, sonication does not notably affect the surface topography of this mineral (see Figure S9 in the Supporting Information for more details). Rather, the large dissolution enhancement exhibited by albite is on account of its low surface energy (see Figure 1f). This illustrates the importance of simultaneously considering the surface energy and stacking fault energy to understand the effect of sonication on minerals' reactivity.

Overall, these results indicate that atomic dislocations and fracture (bond rupture) are the two primary mechanisms by which sonication increases dissolution kinetics. This indicates that the effect of sonication on the dissolution rate of a given mineral is governed by (i) its surface energy (i.e., which controls its propensity to break) and (ii) its stacking fault energy (i.e., which controls its propensity to produce and tolerate plastic dislocations). It should be noted that surface energy and stacking fault energy are largely independent of each other (see Figure S6); therefore, these properties capture two distinct contributions of the sonication-induced enhancement in the dissolution kinetics.

Theoretical Framework. Our experimental data and simulations suggest that both bond breaking and dislocations synergistically contribute to the increase in dissolution rates that is observed under acoustic stimulation. Based on these observations, we propose a new theoretical framework that accounts for this dual mechanism (see Figure 3). First, the collapse of cavitation bubbles in proximity to mineral surfaces results in shock waves or microjets, which locally generate high stresses on mineral surfaces; i.e., due to the "water hammer" effect.⁴² Due to the stochastic nature of the size, internal pressure, anisotropy, and collapse time of the cavitation bubbles, the resulting shock energy that is imposed on the mineral surface exhibits some variability. 43 Here, for simplicity, we assume for the frequency and power of acoustic stimulation applied herein (20 kHz, 30 W) that the shock energy follows a Gaussian distribution (see Figure 4a). Since the sonication frequency and power are fixed, the average value μ and standard deviation σ of the shock energy distribution are invariant and do not depend on the solute. Note that the parameters μ and σ are not easily assessed a priori and, herein,

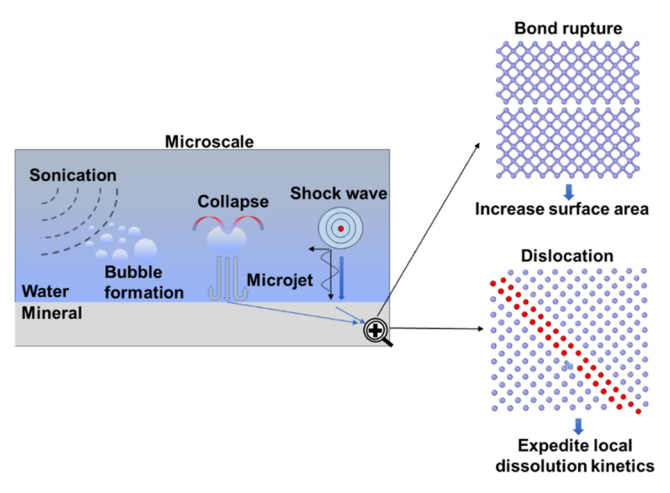


Figure 3. Illustration of the atomistic mechanism of dissolution amplification under acoustic stimulation.

are determined *a posteriori* by fitting the experimental data of sonication-induced dissolution enhancement (see below).

Based on the shock energy distribution, a given fraction of the cavitation bubbles will successfully activate fracture or dislocation effects (i.e., if the shock energy is large enough). The probability for such activation is determined by comparing the shock energy distribution to the threshold energies that are needed to activate fracture and dislocation, namely, the surface energy $\gamma_{\rm surf}$ and stacking fault energy $\gamma_{\rm stack}$, respectively (see Figure 4a). The probabilities to trigger fracture ($p_{\rm frac}$) and dislocation ($p_{\rm dis}$) effects are then obtained by analytically integrating the Gaussian distribution starting from the threshold energy, i.e., the minimum energy that is needed to activate fracture or dislocations

$$p_{\text{frac}} = \left(\frac{1}{2} - \frac{1}{2} \text{erf} \left(\frac{\gamma_{\text{surf}} - \mu}{\sigma \sqrt{2}}\right)\right)$$
 (2a)

$$p_{\text{dis}} = \left(\frac{1}{2} - \frac{1}{2} \operatorname{erf}\left(\frac{\gamma_{\text{stack}} - \mu}{\sigma \sqrt{2}}\right)\right) \tag{2b}$$

where erf() is the error function.

We first focus on fracture. To the first order, the increase in the dissolution kinetics arising from fracture is simply related to the associated increase in exposed surface area. Assuming that the resulting fracture pattern (i.e., that results when the cavitation energy exceeds the surface energy of a given solute) does not depend on the considered solute, the relative increase in the dissolution rate $(D_r^{\rm frac})$ resulting from the increase in surface area due to fracture is given by

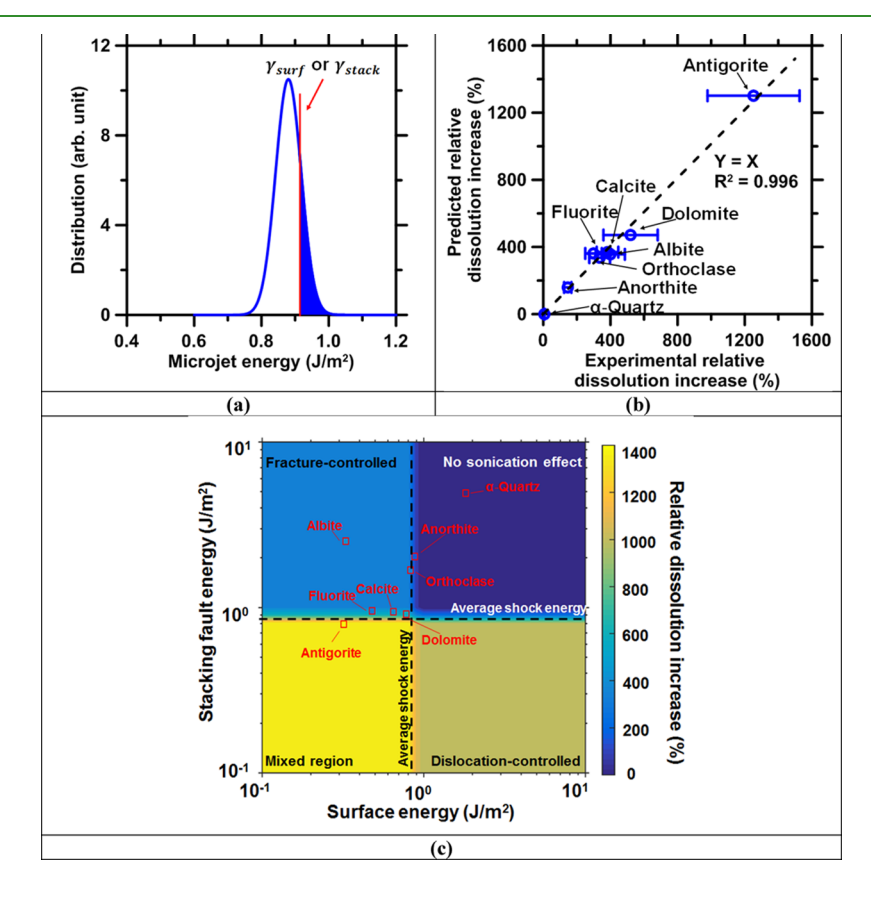


Figure 4. Combined effects of bond breaking and dislocation on dissolution enhancement. (a) Probability distribution of the microjet energy resulting from the collapse of cavitation bubbles, as inferred from eq 5. The red vertical line indicates the surface or stacking fault energy for a given solute, which is used as a threshold to calculate the probability for a cavitation bubble to activate a fracture or dislocation event (represented by the blue region). (b) Comparison between the sonication-induced increase in dissolution rate predicted by our model and experimental data. The y = x dashed line indicates a perfect agreement. The error bars represent the standard deviation. (c) Relative increase in dissolution rate (color scale) as a function of both surface energy and stacking fault energy. The positions on this map of all the minerals considered herein are indicated by square symbols, with their experimentally measured relative dissolution increase indicated using the color scale.

$$D_{\rm r}^{\rm frac} = D_{\rm l} \left(\frac{1}{2} - \frac{1}{2} \operatorname{erf} \left(\frac{\gamma_{\rm surf} - \mu}{\sigma \sqrt{2}} \right) \right) \tag{3}$$

where D_1 is a nondimensional constant that captures the increase in exposed surface area resulting from a single fracture event.

We then focus on dislocation events. Previous studies have noted that increasing dislocation density tends to increase minerals' dissolution kinetics by affecting their Gibbs free energy. 38,44,45 However, at this time, we note that no direct, quantitative relationship exists between dislocation density and associated dissolution enhancement. For simplicity, we assume that the dissolution enhancement $(D_{\rm r}^{\rm dis})$ resulting from dislocation events is proportional to the density of surface dislocations as follows

$$D_{\rm r}^{\rm dis} = D_2 \left(\frac{1}{2} - \frac{1}{2} \operatorname{erf} \left(\frac{\gamma_{\rm stack} - \mu}{\sigma \sqrt{2}} \right) \right) \tag{4}$$

where D_2 is a nondimensional constant that captures how much a single dislocation feature increases the dissolution rate (i.e., which is assumed to be similar for all minerals; a conservative assumption). Thus, taken together, the total dissolution enhancement resulting from these two mechanisms can be expressed as

$$D_{\rm r} = D_{\rm r}^{\rm frac} + D_{\rm r}^{\rm dis} \tag{5}$$

This analytical basis yields four currently unknown parameters (i.e., D_1 , D_2 , μ , and σ), wherein the parameters μ and σ are the average and standard deviations of the shock energy distribution. The energy of shock waves emitted by a single collapsing bubble is reported to be up to tens of mJ and is dependent on the anisotropy parameter, i.e., the dimensionless equivalent of the Kelvin impulse. 4,46,47 However, experimentally measured distributions of shock energies, e.g., as shown in Figure 4a, strongly depend on the system and process parameters. 48 Therefore, we ascertain these four parameters $(D_1, D_2, \mu, \text{ and } \sigma)$ by fitting eq 5 to our experimental dissolution enhancement data (D_r) across all minerals considered using a least squares method—i.e., by solving eight equations with four unknowns that are the same across all minerals: D_1 (3.5, unitless), D_2 (9.5, unitless), μ (0.88 J/m²), and σ (0.038 J/m²). Note that due to the nonlinear nature of the error function, this fitting is carried out using the trust-region-reflective and Monte Carlo algorithms^{49,50} to ensure that the optimization is not trapped in a local minimum. Figure 4a shows the distribution of the microjet energy a posteriori inferred from this fitting. To assess the accuracy of this model, Figure 4b shows the comparison between the sonication-induced increase in dissolution rates estimated by eq 5 and the experimental values presented in Table 1. In general, we observe excellent agreement between predicted and experimental values—with a coefficient of determination R^2 of 0.996. This supports the ability of our model to offer a realistic description of sonication-induced dissolution enhancement.

Also shown in Figure 4c is the combined influence of surface energy and stacking fault energy on the relative increase in dissolution kinetics, which properly explains, for the first time, our collective experimental observations. For instance, the difference in surface energy explains why albite is more affected by sonication than anorthite (despite their fairly similar stacking fault energy), while the difference in stacking fault

energy explains why antigorite is more affected than albite (despite their fairly similar surface energy). Overall, as shown in Figure 4c, diverse minerals can be classified into four categories based on the dominant underlying mechanism. First, albite exhibits a combination of high stacking fault energy and moderate surface energy—as compared to the average shock energy (μ) for the nature of acoustic stimulation applied herein (dotted line)—so that the sonication-induced dissolution enhancement observed for this mineral is primarily governed by fracture ("fracture-controlled" region in Figure 4c). In contrast, minerals exhibiting a combination of high surface energy and moderate stacking fault energy would be primarily governed by dislocation events ("dislocation-controlled" region in Figure 4c). No example of such mineral is found herein. In between these extreme cases, antigorite simultaneously shows moderate values of surface energy and stacking fault energy. As such, for antigorite, sonication-induced dissolution enhancement is simultaneously governed by fracture and dislocation events ("mixed region" in Figure 4c). Finally, in contrast, quartz exhibits a combination of high surface energy and stacking fault energy and, hence, is only very weakly affected by sonication ("no sonication effect" in Figure 4c). This classification is less clear in the case of anorthite and orthoclase, which present a surface energy that is close to the average shock energy. Similarly, calcite, dolomite, and fluorite exhibit a stacking fault energy that is close to the average shock energy and, hence, are located at the boundary between the "fracture-controlled" and "mixed" regions. Overall, the "acoustic stimulation map" presented in Figure 4c offers a convenient representation to quickly estimate whether the dissolution kinetics of a given mineral is likely to be affected by sonication and, if so, which mechanism is expected to be predominant. Expectedly, however, this analytical framework does not yet account for second-order features of minerals that may affect their dissolution rates, e.g., point defects, chemical impurities, porosity, etc.

Finally, we explore whether the effect of sonication on reactivity could in some ways be directly encoded in the nature of the interatomic bonds the minerals are made of. As shown in Figure S10 in the Supporting Information, we observe the existence of a strong (inverse) correlation between the average bond energy (calculated over the cleavage plane of each mineral) and dissolution enhancement. This is not surprising since the average bond energy is reflected in the surface energy of the minerals. However, we do not observe any obvious correlation between the average degree of covalency of the bonds (calculated over the slip plane of each mineral) and dissolution enhancement (see Figure S11 in the Supporting Information). This suggests that the ionic vs covalent nature of the interatomic bonds (and their degree of directionality) in minerals does not have a first-order effect on their sensitivity to sonication. Overall, the fact that dissolution enhancement exhibits a stronger correlation with surface energy and stacking fault energy (as compared to bond energy and degree of covalency) suggests that besides the nature of the interatomic bonds in minerals, the atomic structure itself also plays an important role in governing dissolution enhancement upon sonication. In that regard, as macroscopic materials' properties, the surface energy and stacking fault energy (which are used as inputs for the present model) simultaneously capture the effects of interatomic bonds and crystalline structure.

CONCLUSIONS

By combining dissolution rate observations and MD simulations, this study reveals two underlying atomic mechanisms that control the increase in dissolution kinetics that are produced across a wide range of minerals following acoustic stimulation. Importantly, we find that dissolution enhancement arises both from fracture and dislocation events. This dual mechanism helps explain previously contrasting conclusions—i.e., since the dominant mechanism depends on the mechanical attributes of the solute considered (i.e., fracture energy vs stacking fault energy). Simultaneously considering both of these mechanisms allows rationalization of available experimental data and introduces a unifying model that explains the roles and extents of these two phenomena during sonication-induced dissolution enhancement. Furthermore, it would be of great value to explicitly simulate by nonequilibrium molecular dynamics simulations the effect of sonication on minerals—which would offer a direct access to the dynamics of bond breaking and dislocation upon shock wave propagation. Such simulations would also enable a direct estimation of the energy that is released from cavitation or nanobubble collapse. In that regard, the availability of a universal reactive force field that could model all the minerals considered herein (and their interaction with the solution) while relying on a consistent parameterization would be key.

The ability to enhance the dissolution kinetics of minerals using electrically driven acoustic fields (e.g., that are powered by renewable energy) would be of great value in numerous applications wherein mineral (solute) reactivity is a bottleneck. In addition, understanding the underlying features that affect rate enhancement (or not) would be foundational to unlock green chemistry approaches for several applications. For example, enhancing the dissolution rate of minerals is of critical importance to increase the efficiency of CO2 mineralization applications.⁵⁴ Accelerating the dissolution of minerals could also be key to bypass the need for hightemperature clinkering during the manufacturing of cementing agents-which is the main contribution to concrete's embodied CO₂.⁵⁵ Finally, sonication offers a promising pathway to accelerate the dissolution of industrial waste byproducts (e.g., fly ash or slag), which could facilitate their recycling and beneficial use-which is key to create a meaningful circular economy for industrial waste.

However, the cost and energy efficiency of sonication must be compared with alternative approaches (e.g., accelerating dissolution by increasing temperature or the use of reagents) to ensure practical feasibility. The outcomes of this study offer original insights to assess for which minerals sonication may be the most effective. For instance, minerals characterized with high surface energy and stacking fault energy are only very weakly affected by sonication—which limits the potential of this approach for such minerals. However, for other minerals, sonication results in notable enhancements in dissolution kinetics without the need to externally increase the reaction temperature (although this may indeed accompany sonication for nonthermostated systems). As such, sonication offers a promising route to stimulate reactivity in a cost- and energyefficient manner.⁵¹ It should be noted that this study focuses on room-temperature dissolution (i.e., 300 K). However, temperature could offer an additional degree of freedom to tune the efficiency of sonication for a given material. For instance, many phases exhibit a decrease in their stacking fault

energy with even small increases in temperature, ^{52,53} which, in turn, would increase the efficiency of sonication (i.e., even for minerals that are largely insensitive to sonication at room temperature).

METHODS

Materials. We considered a selection of naturally occurring minerals sourced from Ward's Science. To prepare the particulate samples, all the minerals were ground using a ball mill and then sieved to isolate particles that have a size in the range of 300 to 600 μ m. To prepare planar solute surfaces, the minerals were sectioned (i.e., with dimension smaller than 2 cm) and then embedded in epoxy resin to facilitate handling. The exposed mineral surfaces were polished successively using SiC abrasives and diamond paste and finally polished using a 50 nm colloidal silica suspension. The surface topography maps of as-polished calcite and quartz surfaces used in the dissolution analyses are shown in Figures S3 and S4, respectively. The calcite and quartz surfaces feature initial root mean square (RMS) roughness (S_a) values of around 5 and 10 nm, respectively.

■ EXPERIMENTAL METHODS

Batch Dissolution. Batch dissolution experiments were conducted in a manner similar to Wei *et al.*¹⁸ by adding 0.1–0.5 g of ground mineral samples into 100 mL of 18 MΩ·cm deionized (DI) water, thereby resulting in solid-to-liquid ratios (s/l) in the range of 1:200 to 1:1000. The solids were reacted with water under isothermal conditions (25 \pm 0.5 °C) for up to 2 h to maintain dissolution in the far-from-equilibrium region, i.e., wherein the amount of solute dissolved yields a linear expression as a function of time. Nonsonicated dissolution analyses were conducted in environmental chambers. Dissolution under conditions of sonication was carried out by circulating cooling water in a water-jacketed batch reactor. ¹⁸ In the case of nonsonicated dissolution, the solution was stirred using a magnetic stirrer at 350 rpm. Sonication was applied using a horn-type ultrasonic system (Fisher Scientific 505 Sonic Dismembrator; 500 W; 1/2 in. tip diameter) operating at a constant ultrasonic power of 30 W.

Over the course of dissolution, the solutions were sampled at different time intervals and diluted in 5% (v/v) HNO₃ for elemental analysis following filtration through a 0.2 μ m filter. The elemental analysis was carried out using a PerkinElmer Avio 200 inductively coupled plasma-optical emission spectrometer, with calibration standards prepared from concentrated (1000 ppm) standards (Inorganic Ventures). Dissolution rates are calculated based on a linear fitting of the concentration—time profiles. The dissolution rate is averaged over two independent measurements, which has been found to be large enough for monophasic minerals. The uncertainty in the dissolution rates is determined based on two replicated experiments, which, on average, yields an uncertainty of 15 and 10% for nonsonicated and sonicated conditions, respectively.

Particulate Analysis. The particle size distributions (PSDs) of the particulate samples were measured using an LS13-320 Beckman Counter static light scattering analyzer based on three replicate experiments. One gram of ground and sieved particulates for each mineral species was analyzed prior to dissolution to obtain their particle size. The median diameter d_{50} and the specific surface area (SSA) of the samples, estimated based on the assumption of spherical particulates, are presented in Table S2. It is noted that antigorite forms sheet-like grains upon grinding (see Figure S1) so that for this mineral, the spherical assumption may lead to inaccurate median diameter and SSA values. However, this assumption should not impact the measured relative dissolution enhancement data (eq 1). Following a desired period of dissolution, the particulates were retrieved from the reaction solution using a sieve with a 10 μm opening and subsequently examined using (a) light microscopy (Leica DM750P) and (b) light scattering to assess changes in the particle size and/or surface morphology following dissolution under nonsonicated or sonicated conditions. For augmented morphology analysis, the dried particulates were dipped and attached to adhesive

carbon tape and characterized using a Phenom G-2 scanning electron microscope.

Surface Topography Characterization. The topographies of dissolving surfaces were examined using a Zygo NewView 8200 vertical scanning interferometer. A 50× Mirau objective (numerical aperture, NA = 0.55) was used that yields a lateral resolution of 0.16 μ m and a vertical resolution on the order of 2 nm. The three-dimensional (3D) topography data were analyzed using Gwyddion (v2.54) and MATLAB R2017b. ^{56,57}

■ MOLECULAR DYNAMICS SIMULATIONS

Force Field. We carried out a series of molecular dynamics (MD) simulation to compute select mechanical properties of the minerals considered herein. In general, the accuracy of MD simulations largely depends on that of the interatomic force field. Although using a universal interatomic potential for all the minerals would be desirable, such a force field is not presently available for the wide variety of the minerals selected herein (i.e., silicates, carbonates, etc.). Rather, here, we selected two types of interatomic potentials based on their ability to offer a realistic prediction of the structure and properties of the minerals. On the one hand, we selected a Buckingham-based potential for fluorite, 58 calcite, 59 and dolomite 59—wherein the force field parameters can be found in each relevant reference. On the other hand, we adopted the ClayFF classical force field⁶⁰ for the other minerals. In both cases, Coulombic interactions are resolved by using the particle-particle particle-mesh (PPPM) method.⁶¹ Each system comprises about 2000 to 9000 atoms (depending on the size of the unit cell), which is found to be large enough to avoid any spurious finite-size effect (see Figure S12 in the Supporting Information for more details). Periodic boundary conditions are employed along all directions, except for the calculation of stacking fault energy (see below). All of the simulations are performed with the open source molecular dynamics code LAMMPS.⁶²

To validate our MD results, we first ensured that the crystalline structure at 300 K of the minerals considered herein is well described (i.e., vis-à-vis experimental observations) by the selected force fields. Toward this end, starting from initial crystal structures sourced from experiments (see Table S4), each crystal was equilibrated at 1 K and zero pressure for 1 ns. Then, the equilibrated structures were further relaxed at 300 K and zero pressure for an additional 1 ns. All simulations were conducted in the isothermal-isobaric (NPT) ensemble, wherein both the box length and tilt angles were free to change to ensure a zero stress in all directions. The Nosé-Hoover thermostat 63,64 was used for temperature control. For all simulations, the time step was fixed at 1 fs. To filter out the effect of thermal fluctuations, all of the computed properties were averaged over 100 ps of statistical averaging after full equilibration. As shown in Figure S7, the mineral densities calculated from the MD simulations agree well with experimental data. Moreover, the relative errors of the predicted lattice constants are well below 3.5% (see Table S4). These results indicate that our MD simulations are able to offer a realistic prediction of the structures of all the minerals considered herein.

It should be noted that force fields are typically parameterized based on equilibrium bulk properties and do not always perform well when used to predict more complex properties (e.g., surface energy or stacking fault energy). Here, to assess the level of accuracy of the force fields in predicting such properties, we compared the simulated surface energy obtained for quartz with available experimental results.

Available experimental data suggest that the surface energy data of quartz range from 1.8 to 2.4 J/m^2 depending on the surface orientation, while our simulation data range from 1.82 to 2.93 J/m^2 . The surface energy along the [001] cleavage plane was found to be 2.23 J/m^2 based on *ab initio* simulations, which is fairly close to the value obtained herein (i.e., 1.82 J/m^2). This suggests that the force field selected herein offers reasonable predictions of the surface energy of quartz. We also compared the simulated surface energy obtained for fluorite along its cleavage plane (i.e., [111] plane) with available results from *ab initio* simulations. We find that the surface energy predicted by the present force field (i.e., 0.48 J/m^2) indeed exhibits a close match with the *ab initio* data (i.e., 0.47 J/m^2).

Calculation of Surface Energy. To calculate the surface energy, the equilibrated crystals were first cut along a given plane into two parts by switching off the interactions between atoms across the plane. Then, the cut system was further relaxed at zero pressure for equilibration. The surface energy $\gamma_{\rm surf}$ associated with this plane was calculated as $\Delta U/\Delta A$, where ΔU is the variation in the potential energy of equilibrated structures before and after cleaving, while ΔA is the surface area created by the cleavage. To identify the cleavage plane, we first selected a series of tentative plane orientations (all the plane orientations considered herein are listed in Table S3 in the Supporting Information). Then, we systematically attempted to cut the system into two parts along varying plane locations. Since cracks preferentially initiate and propagate along the weakest plane, we then identified the cleavage plane as the one featuring the lowest surface energy (i.e., which characterizes the plane that exhibits the lowest/ weakest cohesion within the mineral). For statistical purposes, the surface energy is obtained by averaging the results from three independent simulations.

Calculation of Stacking Fault Energy. The stacking fault energy characterizes the energy barrier that needs to be overcome to activate a stacking fault defect, which plays an important role in dislocation formation of minerals. ⁴¹ The computation of the stacking fault energy was performed as follows. Starting from the equilibrated crystal structure, the structure was relaxed toward its inherent configuration (i.e., the local minimum position in the energy landscape) by using the conjugate gradient algorithm. The boundary conditions were set as a free boundary along the direction that is perpendicular to the selected slip plane and periodic along the other two directions (with fixed length). During the stacking fault calculation, the two halves of the crystal are rigidly laterally displaced with respect to each other along the slip plane. In detail, the upper part of the system is gradually displaced along the slip line with an increment of 0.1 Å, while the lower part was kept fixed. After each displacement increment, the crystal is allowed to relax in the direction that is orthogonal to the slip plane using the conjugate gradient algorithm (while the atomic coordinates remain frozen along the two other directions). We then tracked the evolution of the energy of the system as a function of the slip plane displacement. The stacking fault energy γ_{stack} of the selected slip plane was then calculated from the difference between the maximum potential energy achieved during the deformation and that of the equilibrium configuration (i.e., before any deformation). Similar to the surface energy, we calculated the stacking fault energy along a large number of slip planes (see Table S4 in the Supporting Information for more details) and identified the slip plane as

the one featuring the lowest stacking fault energy (i.e., along which dislocation formation is energetically preferred). For statistical purposes, the stacking fault energy is also obtained by averaging the results obtained from three independent simulations.

Calculation of the Average Bond Energy. The average bond energy $S_{\rm bond}$ is calculated based on the dissociation enthalpy D° of each bond crossing the cleavage plane as $S_{\rm bond} = \sum_{i=1}^{N} x_i D^{\circ}$, where N is the total number of chemical bond types on the cleavage plane, i represents the type of chemical bond, and x_i are the fractions of each type of bond. The dissociation enthalpy D° values are obtained from ref 68.

Calculation of the Average Degree of Covalency. The average degree of covalency $f_{\rm cov}$ of the bonds crossing the slip plane of each mineral is calculated as $f_{\rm cov} = \sum_{i=1}^N x_i \exp(-0.25\Delta E_i^2)$, where N is the total number of chemical bond types on the slip plane, i represents the type of chemical bond, x_i are the fractions of each type of bond, and ΔE_i is the associated difference in the electronegativity of the pair of elements forming the bond.

ASSOCIATED CONTENT

Supporting Information

The Supporting Information is available free of charge at https://pubs.acs.org/doi/10.1021/acsami.0c16424.

Details and validation of the molecular dynamics simulations; polarized light microscopy images of solute particulates, cumulative volume distribution of calcite particulates, and topography images of as-polished calcite and quartz; effect of the bond energy and the degree of covalency of the bonds on the dissolution enhancement (PDF)

AUTHOR INFORMATION

Corresponding Authors

Gaurav Sant — Laboratory for the Chemistry of Construction Materials (LC2), Department of Civil and Environmental Engineering, Department of Materials Science and Engineering, Institute for Carbon Management (ICM), and California Nanosystems Institute (CNSI), University of California, Los Angeles, California 90095, United States; orcid.org/0000-0002-1124-5498; Email: gsant@ucla.edu

Mathieu Bauchy — Physics of AmoRphous and Inorganic Solids Laboratory (PARISlab), Department of Civil and Environmental Engineering and Institute for Carbon Management (ICM), University of California, Los Angeles, California 90095, United States; orcid.org/0000-0003-4600-0631; Email: bauchy@ucla.edu

Authors

Longwen Tang – Physics of AmoRphous and Inorganic Solids Laboratory (PARISlab), Department of Civil and Environmental Engineering, University of California, Los Angeles, California 90095, United States

Shiqi Dong – Laboratory for the Chemistry of Construction Materials (LC2), Department of Civil and Environmental Engineering, Department of Materials Science and Engineering, and Institute for Carbon Management (ICM), University of California, Los Angeles, California 90095, United States

- Ross Arnold Laboratory for the Chemistry of Construction Materials (LC2), Department of Civil and Environmental Engineering and Institute for Carbon Management (ICM), University of California, Los Angeles, California 90095, United States
- Erika Callagon La Plante Department of Materials Science and Engineering, University of Texas at Arlington, Arlington, Texas 76019, United States; orcid.org/0000-0002-5273-9523
- Juan Carlos Vega-Vila Institute for Carbon Management (ICM) and Department of Chemical and Biomolecular Engineering, University of California, Los Angeles, California 90095, United States
- Dale Prentice Laboratory for the Chemistry of Construction Materials (LC2), Department of Civil and Environmental Engineering and Institute for Carbon Management (ICM), University of California, Los Angeles, California 90095, United States
- Kirk Ellison Electric Power Research Institute (EPRI), Charlotte, North Carolina 28262-8550, United States
- Aditya Kumar Department of Materials Science and Engineering, Missouri University of Science and Technology, Rolla, Missouri 65409, United States; occid.org/0000-0001-7550-8034
- Narayanan Neithalath School of Sustainable Engineering and the Built Environment, Arizona State University, Tempe, Arizona 85281, United States
- Dante Simonetti Institute for Carbon Management (ICM) and Department of Chemical and Biomolecular Engineering, University of California, Los Angeles, California 90095, United States; orcid.org/0000-0002-5708-460X

Complete contact information is available at: https://pubs.acs.org/10.1021/acsami.0c16424

Author Contributions

[&]L.T. and S.D. contributed equally to this work. The manuscript was written through contributions of all authors. All authors have given approval to the final version of the manuscript.

Notes

The authors declare no competing financial interest.

ACKNOWLEDGMENTS

The authors acknowledge financial support for this research provisioned by Department of Energy's Advanced Research Projects Agency for Energy (ARPA-E; award number: DE-AR0001147), U.S. National Science Foundation (DMREF-1922167), and the Electric Power Research Institute. The contents of this paper reflect the views and opinions of the authors, who are responsible for the accuracy of data presented. This research was carried out in the Laboratory for the Chemistry of Construction Materials (LC2), Physics of AmoRphous and Inorganic Solids Laboratory (PARISlab), and Molecular Instrumentation Center at UCLA. As such, the authors gratefully acknowledge the support that has made these laboratories and their operations possible. The authors gratefully acknowledge Dr. Joseph King (ARPA-E) and Prof. Seth Putterman (UCLA) for numerous discussions on the mechanisms of acoustic stimulation.

REFERENCES

- (1) Wei, Z.; Villamena, F. A.; Weavers, L. K. Kinetics and Mechanism of Ultrasonic Activation of Persulfate: An in Situ EPR Spin Trapping Study. *Environ. Sci. Technol.* **2017**, *51*, 3410–3417.
- (2) Suslick, K. S. Sonochemistry. Science 1990, 247, 1439-1445.
- (3) Pecha, R.; Gompf, B. Microimplosions: Cavitation Collapse and Shock Wave Emission on a Nanosecond Time Scale. *Phys. Rev. Lett.* **2000**, *84*, 1328–1330.
- (4) Supponen, O.; Obreschkow, D.; Kobel, P.; Tinguely, M.; Dorsaz, N.; Farhat, M. Shock Waves from Nonspherical Cavitation Bubbles. *Phys. Rev. Fluids* **2017**, *2*, No. 093601.
- (5) Chen, Y. L.; Israelachvili, J. New Mechanism of Cavitation Damage. Science 1991, 252, 1157–1160.
- (6) Holian, B. L.; Lomdahl, P. S. Plasticity Induced by Shock Waves in Nonequilibrium Molecular-Dynamics Simulations. *Science* **1998**, 280, 2085–2088.
- (7) Escaler, X.; Egusquiza, E.; Farhat, M.; Avellan, F.; Coussirat, M. Detection of Cavitation in Hydraulic Turbines. *Mechanical Systems and Signal Processing* **2006**, *20*, 983–1007.
- (8) Vogel, A.; Lauterborn, W.; Timm, R. Optical and Acoustic Investigations of the Dynamics of Laser-Produced Cavitation Bubbles near a Solid Boundary. *J. Fluid Mech.* **1989**, *206*, 299–338.
- (9) Sancheti, S. V.; Gogate, P. R. A Review of Engineering Aspects of Intensification of Chemical Synthesis Using Ultrasound. *Ultrason. Sonochem.* **2017**, *36*, 527–543.
- (10) Pawar, S. V.; Rathod, V. K. Ultrasound Assisted Process Intensification of Uricase and Alkaline Protease Enzyme Co-Production in Bacillus Licheniformis. *Ultrason. Sonochem.* **2018**, *45*, 173–179.
- (11) Shirsath, S. R.; Sonawane, S. H.; Gogate, P. R. Intensification of Extraction of Natural Products Using Ultrasonic Irradiations—A Review of Current Status. *Chem. Eng. Process.: Process Intesif.* **2012**, *53*, 10–23.
- (12) Sillanpää, M.; Pham, T.-D.; Shrestha, R. A. Ultrasound Technology in Green Chemistry. In *Ultrasound Technology in Green Chemistry*; Sillanpää, M., Ed.; SpringerBriefs in Molecular Science; Springer Netherlands: Dordrecht, 2011; pp. 1–21, DOI: 10.1007/978-94-007-2409-9 1.
- (13) Krevor, S. C. M.; Lackner, K. S. Enhancing Serpentine Dissolution Kinetics for Mineral Carbon Dioxide Sequestration. *Int. J. Greenhouse Gas Control* **2011**, *5*, 1073–1080.
- (14) Ragipani, R.; Bhattacharya, S.; Suresh, A. K. Towards Efficient Calcium Extraction from Steel Slag and Carbon Dioxide Utilisation via Pressure-Swing Mineral Carbonation. *React. Chem. Eng.* **2019**, *4*, 52–66.
- (15) Shchukin, D. G.; Skorb, E.; Belova, V.; Möhwald, H. Ultrasonic Cavitation at Solid Surfaces. *Adv. Mater.* **2011**, *23*, 1922–1934.
- (16) Gogate, P. R. Cavitational Reactors for Process Intensification of Chemical Processing Applications: A Critical Review. *Chem. Eng. Process.: Process Intesif.* **2008**, 47, 515–527.
- (17) Didenko, Y. T.; McNamara, W. B.; Suslick, K. S. Hot Spot Conditions during Cavitation in Water. J. Am. Chem. Soc. 1999, 121, 5817–5818.
- (18) Wei, Z.; Hsiao, Y.-H.; Chen, X.; La Plante, E. C.; Mehdipour, I.; Simonetti, D.; Neithalath, N.; Pilon, L.; Bauchy, M.; Israelachvili, J.; Sant, G. Isothermal Stimulation of Mineral Dissolution Processes by Acoustic Perturbation. *J. Phys. Chem. C* **2018**, *122*, 28665–28673.
- (19) Párez-Maqueda, L. A.; Franco, F.; Avilés, M. A.; Poyato, J.; Pérez-Rodríguez, J. L. Effect of Sonication on Particle-Size Distribution in Natural Muscovite and Biotite. *Clays Clay Miner.* **2003**, *51*, 701–708.
- (20) Birkin, P. R.; Silva-Martinez, S. A Study of the Effect of Ultrasound on Mass Transport to a Microelectrode. *J. Electroanal. Chem.* **1996**, *416*, 127–138.
- (21) Kannan, A.; Pathan, S. K. Enhancement of Solid Dissolution Process. *Chem. Eng. J.* **2004**, *102*, 45–49.
- (22) Tanguy, D.; Mareschal, M.; Lomdahl, P. S.; Germann, T. C.; Holian, B. L.; Ravelo, R. Dislocation Nucleation Induced by a Shock

- Wave in a Perfect Crystal: Molecular Dynamics Simulations and Elastic Calculations. *Phys. Rev. B* **2003**, *68*, 144111.
- (23) Germann, T. C.; Holian, B. L.; Lomdahl, P. S.; Ravelo, R. Orientation Dependence in Molecular Dynamics Simulations of Shocked Single Crystals. *Phys. Rev. Lett.* **2000**, *84*, 5351–5354.
- (24) Adhikari, U.; Goliaei, A.; Berkowitz, M. L. Mechanism of Membrane Poration by Shock Wave Induced Nanobubble Collapse: A Molecular Dynamics Study. *J. Phys. Chem. B* **2015**, *119*, 6225–6234.
- (25) Vedadi, M.; Choubey, A.; Nomura, K.; Kalia, R. K.; Nakano, A.; Vashishta, P.; van Duin, A. C. T. Structure and Dynamics of Shock-Induced Nanobubble Collapse in Water. *Phys. Rev. Lett.* **2010**, *105*, No. 014503
- (26) Brobst, D. A.; Pratt, W. P. Geological Survey Professional Paper; U.S. Government Printing Office: 1973.
- (27) McCarthy, N. A.; Kelly, P. M.; Maher, P. G.; Fenelon, M. A. Dissolution of Milk Protein Concentrate (MPC) Powders by Ultrasonication. *J. Food Eng.* **2014**, *126*, 142–148.
- (28) King, A. J.; Readman, J. W.; Zhou, J. L. Determination of Polycyclic Aromatic Hydrocarbons in Water by Solid-Phase Microextraction—Gas Chromatography—Mass Spectrometry. *Anal. Chim. Acta* **2004**, 523, 259—267.
- (29) Wagterveld, R. M.; Boels, L.; Mayer, M. J.; Witkamp, G. J. Visualization of Acoustic Cavitation Effects on Suspended Calcite Crystals. *Ultrason. Sonochem.* **2011**, *18*, 216–225.
- (30) Tang, X.; Liu, M.; Tang, Q.; Du, Z.; Bai, S.; Zhu, Y. Effect of Ultrasound on the Dissolution of Magnesium Hydroxide: PH-Stat and Nanoscale Observation. *Ultrason. Sonochem.* **2019**, *55*, 223–231.
- (31) Doktycz, S. J.; Suslick, K. S. Interparticle Collisions Driven by Ultrasound. *Science* **1990**, 247, 1067–1069.
- (32) Suslick, K. S.; Nyborg, W. L. Ultrasound: Its Chemical, Physical and Biological Effects. *J. Acoust. Soc. Am.* **1990**, *87*, 919.
- (33) Griffith, A. A. VI. The Phenomena of Rupture and Flow in Solids. *Philos. Trans. R. Soc. London, Ser. A* 1921, 221, 163–198.
- (34) Bibi, I.; Arvidson, R. S.; Fischer, C.; Lüttge, A. Temporal Evolution of Calcite Surface Dissolution Kinetics. *Minerals* **2018**, *8*, 256.
- (35) Lasaga, A. C.; Luttge, A. Variation of Crystal Dissolution Rate Based on a Dissolution Stepwave Model. *Science* **2001**, *291*, 2400–2404.
- (36) Brantley, S. L. Kinetics of Mineral Dissolution. In *Kinetics of Water-Rock Interaction*; Brantley, S. L., Kubicki, J. D., White, A. F., Eds.; Springer: New York, NY, 2008; pp. 151–210, DOI: 10.1007/978-0-387-73563-4 5.
- (37) Dove, P. M.; Han, N.; de Yoreo, J. J. Mechanisms of Classical Crystal Growth Theory Explain Quartz and Silicate Dissolution Behavior. *PNAS* **2005**, *102*, 15357–15362.
- (38) Blum, A. E.; Yund, R. A.; Lasaga, A. C. The Effect of Dislocation Density on the Dissolution Rate of Quartz. *Geochim. Cosmochim. Acta* **1990**, *54*, 283–297.
- (39) Tromans, D.; Meech, J. A. Enhanced Dissolution of Minerals: Stored Energy, Amorphism and Mechanical Activation. *Miner. Eng.* **2001**, *14*, 1359–1377.
- (40) MacInnis, I. N.; Brantley, S. L. The Role of Dislocations and Surface Morphology in Calcite Dissolution. *Geochim. Cosmochim. Acta* 1992, 56, 1113–1126.
- (41) Rice, J. R.; Thomson, R. Ductile versus Brittle Behaviour of Crystals. *Philos. Mag.* **1974**, *29*, 73–97.
- (42) Plesset, M. S., Chapman, R. B. Collapse of an Initially Spherical Vapour Cavity in the Neighbourhood of a Solid Boundary. *J. Fluid Mech.* **1971**, *47*, 283–290.
- (43) Brotchie, A.; Grieser, F.; Ashokkumar, M. Effect of Power and Frequency on Bubble-Size Distributions in Acoustic Cavitation. *Phys. Rev. Lett.* **2009**, *102*, No. 084302.
- (44) Xu, J.; Fan, C.; Teng, H. H. Calcite Dissolution Kinetics in View of Gibbs Free Energy, Dislocation Density, and PCO2. *Chem. Geol.* **2012**, 322-323, 11–18.

- (45) Schott, J.; Brantley, S.; Crerar, D.; Guy, C.; Borcsik, M.; Willaime, C. Dissolution Kinetics of Strained Calcite. *Geochim. Cosmochim. Acta* 1989, 53, 373–382.
- (46) Blake, J. R.; Leppinen, D. M.; Wang, Q. Cavitation and Bubble Dynamics: The Kelvin Impulse and Its Applications. *Interface Focus* **2015**, *5*, 20150017.
- (47) Blake, J. R. The Kelvin Impulse: Application to Cavitation Bubble Dynamics. *ANZIAM J.* **1988**, *30*, 127–146.
- (48) Hosny, D. M.; Tibbetts, D.; Luenz, R. Cavitation Intensity Measurements for Internal Combustion Engines. *SAE Trans* **1996**, 105, 1390–1406.
- (49) Conn, A. R.; Scheinberg, K.; Vicente, L. N. Society for Industrial and Applied Mathematics. *Introduction to Derivative-Free Optimization*; MOS-SIAM Series on Optimization, 2009, DOI: 10.1137/1.9780898718768.
- (50) Barlow, R.; Beeston, C. Fitting Using Finite Monte Carlo Samples. Comput. Phys. Commun. 1993, 77, 219-228.
- (51) Dong, S.; Arnold, R.; La Plante, E. C.; Bustillos, S.; Kumar, A.; Simonetti, D.; Bauchy, M.; Sant, G. Additive-Free Dissolution Enhancement of Industrial Alkaline Wastes Using Acoustic Stimulation. Manuscript in preparation; 2020.
- (52) Wu, X.; Liu, L.; Li, W.; Wang, R.; Liu, Q. Effect of Temperature on Elastic Constants, Generalized Stacking Fault Energy and Dislocation Cores in MgO and CaO. *Comput. Condens. Matter* **2014**, *1*, 38–44.
- (53) Kisel, V. P. Mobility of Dislocations in NaCl Single Crystals at Low Temperatures. I. 77 to 298 K. *Phys. Status Solidi A* **1976**, 36, 297–306.
- (54) Romanov, V.; Soong, Y.; Carney, C.; Rush, G. E.; Nielsen, B.; O'Connor, W. Mineralization of Carbon Dioxide: A Literature Review. *ChemBioEng Rev.* **2015**, *2*, 231–256.
- (55) Purnell, P.; Black, L. Embodied Carbon Dioxide in Concrete: Variation with Common Mix Design Parameters. *Cem. Concr. Res.* **2012**, 42, 874–877.
- (56) Dong, S.; la Plante, E. C.; Chen, X.; Torabzadegan, M.; Balonis, M.; Bauchy, M.; Sant, G. Steel Corrosion Inhibition by Calcium Nitrate in Halide-Enriched Completion Fluid Environments. *npj Mater. Degrad.* **2018**, *2*, 32.
- (57) Dong, S.; Chen, X.; La Plante, E. C.; Gussev, M.; Leonard, K.; Sant, G. Elucidating the Grain-Orientation Dependent Corrosion Rates of Austenitic Stainless Steels. *Mater. Des.* **2020**, *191*, 108583.
- (58) de Leeuw, N. H.; Cooper, T. G. A Computational Study of the Surface Structure and Reactivity of Calcium Fluoride. *J. Mater. Chem.* **2003**, *13*, 93–101.
- (59) Raiteri, P.; Demichelis, R.; Gale, J. D. Thermodynamically Consistent Force Field for Molecular Dynamics Simulations of Alkaline-Earth Carbonates and Their Aqueous Speciation. *J. Phys. Chem. C* 2015, *119*, 24447–24458.
- (60) Cygan, R. T.; Liang, J.-J.; Kalinichev, A. G. Molecular Models of Hydroxide, Oxyhydroxide, and Clay Phases and the Development of a General Force Field. *J. Phys. Chem. B* **2004**, *108*, 1255–1266.
- (61) Hockney, R. W. Computer Simulation Using Particles; CRC Press: 1988, DOI: 10.1201/9780367806934.
- (62) Plimpton, S. Fast Parallel Algorithms for Short-Range Molecular Dynamics. J. Comput. Phys. 1995, 117, 1–19.
- (63) Hoover, W. G. Canonical Dynamics: Equilibrium Phase-Space Distributions. *Phys. Rev. A* **1985**, *31*, 1695–1697.
- (64) Nosé, S. A Unified Formulation of the Constant Temperature Molecular Dynamics Methods. *J. Chem. Phys.* **1984**, *81*, 511–519.
- (65) Ball, A.; Payne, B. W. The Tensile Fracture of Quartz Crystals. *J. Mater. Sci.* **1976**, *11*, 731–740.
- (66) Malyi, O. I.; Kulish, V. V.; Persson, C. In Search of New Reconstructions of (001) α -Quartz Surface: A First Principles Study. *RSC Adv.* **2014**, *4*, 55599–55603.
- (67) Puchin, V. E.; Puchina, A. V.; Huisinga, M.; Reichling, M. Theoretical Modelling of Steps on the CaF₂(111) Surface. *J. Phys.: Condens. Matter* **2001**, *13*, 2081–2094.
- (68) Lide, D. R. CRC Handbook of Chemistry and Physics; 85th Edition; CRC Press: 2004.